Pore-scale investigation of mass transport and electrochemistry in a solid oxide fuel cell anode

Kyle N. Grew, Abhijit S. Joshi, Aldo A. Peracchio, Wilson K.S. Chiu*

Department of Mechanical Engineering, University of Connecticut, 191 Auditorium Road, Storrs, CT 06269-3139, United States

ABSTRACT

The development and validation of a model for the study of pore-scale transport phenomena and electrochemistry in a Solid Oxide Fuel Cell (SOFC) anode are presented in this work. This model couples mass transport processes with a detailed reaction mechanism, which is used to model the electrochemical oxidation kinetics. Detailed electrochemical oxidation reaction kinetics, which is known to occur in the vicinity of the three-phase boundary (TPB) interfaces, is discretely considered in this work. The TPB regions connect percolating regions of electronic and ionic conducting phases of the anode, nickel (Ni) and yttria-stabilized zirconia (YSZ), respectively; with porous regions supporting mass transport of the fuel and product. A two-dimensional (2D), multi-species lattice Boltzmann method (LBM) is used to describe the diffusion process in complex pore structures that are representative of the SOFC anode. This diffusion model is discretely coupled to a kinetic electrochemical oxidation mechanism using localized flux boundary conditions. The details of the oxidation kinetics are prescribed as a function of applied activation overpotential and the localized hydrogen and water mole fractions. This development effort is aimed at understanding the effects of the anode microstructure within TPB regions. This work describes the methods used so that future studies can consider the details of SOFC anode microstructure.

© 2009 Elsevier B.V. All rights reserved.

1. Background and introduction

Overpotentials attributed to the oxygen reduction reaction (ORR) in the SOFC cathode have typically driven research efforts aimed at improving the structures and catalysts; however, the anodic electrochemical oxidation reactions can also play a considerable role [1–3]. Recent studies have suggested that losses associated with the reduction processes may be as substantial as those in the cathode, but may be more accessible for optimization and quite important on the overall SOFC performance and durability [2,4–6]. Recent experimental measurements on cells employing advanced composite cathodes supports additional consideration of the anode [3,7,8]. Further, reviews of the pathways and mechanisms of degradation in the SOFC have shown that the anode is quite susceptible to degradation related to the transport (e.g. mass, electronic, ionic, and heat) and activation processes [4,5]. An improved understanding of the coupled transport and electrochemical oxidation processes is needed to provide the scientific insight necessary to address issues such as microstructural optimization and degradation mitigation. The development of a framework for coupling detailed transport and electrochemical reaction kinetics models

within detailed structures representative of the SOFC anode is the focus of this work.

The state of the art SOFC typically consists of a porous Ni–YSZ ceramic–metallic composite (i.e. cermet) anode, thin-film YSZ electrolyte, and porous LSM–YSZ cathode [1]. Electrical work is performed by the extracting the chemical energy that is available in the global reaction,

$$H_2 + \tfrac{1}{2}O_2 \rightarrow H_2O \quad \Delta G_{rxn}\big|_{973\ K} = -194.059 (\text{kJ/mol}) \quad (1)$$
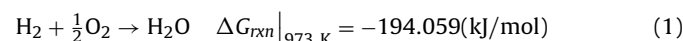
where the change in Gibbs free energy for the global reaction, ΔG_{rxn}, is a measure of the energy available to do work for an ideal system. Here, it is defined at 973 K and atmospheric pressure, a reasonable operating condition for the SOFC, which corresponds to an electromotive force (EMF) of 1.01 V.

In the anode, the electrochemical oxidation of hydrogen, or the hydrogen oxidation reaction (HOR), consumes the fuel (H_2) and an oxide anion (O^{2-}), while producing water vapor (H_2O) and free electrons (e^-). This is expressed as,

$$H_2^{(g)} + O_{electrolyte}^{2-} \rightarrow H_2O^{(g)} + 2e_{Ni}^- \quad (2)$$
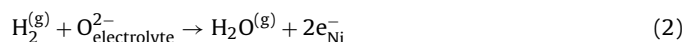
where the (g) superscript denotes the gas phase species, e_{Ni}^- is an electron in the Ni electrode, and $O_{electrolyte}^{2-}$ is an oxygen ion in the YSZ electrolyte. For electrochemical oxidation to occur, an electron conducting phase, oxygen ion conducting phase, and hydrogen molecule all must be in close proximity with continuous

---

* Corresponding author. Tel.: +1 860 486 3647; fax: +1 860 486 5088.
  E-mail address: wchiu@engr.uconn.edu (W.K.S. Chiu).

Nomenclature

C_i	concentration of species i, mol m^{-3}
D_{ij}	binary diffusivity between species i, j, m^2 s^{-1}
F	Faraday's constant, 96,485 A s mol^{-1}
H	domain height, m
i	current density, A m^{-2}
i_0	exchange current density, A m^{-2}
I_i	molecule impingement rate of species i, m^{-2} s^{-1}
J	mole flux, mol m^{-2} s^{-1}
J^*	non-dimensional molar flux
k_{+n}	forward reaction rate constant, s^{-1}
k_{-n}	reverse reaction rate constant, s^{-1}
L	domain length, m
m_i	mass of molecule of species i, kg
M_i	molecular weight of species i, kg kmol^{-1}
n_i	number density species i, m^{-3}
N_A	Avogadro's number, 6.023×10^{23} mol^{-1}
N_0	active site density, m^{-2}
P	pressure, N m^{-2}
r_n	reaction rate n, s^{-1}
R	universal gas constant, 8.314 J mol^{-1} K^{-1}
S	surface site
s_i^0	initial sticking coefficient of species i
t	time, s
T	absolute temperature, K
x^*	dimensionless length $= x/L$
y^*	dimensionless height $= y/H$

Greek

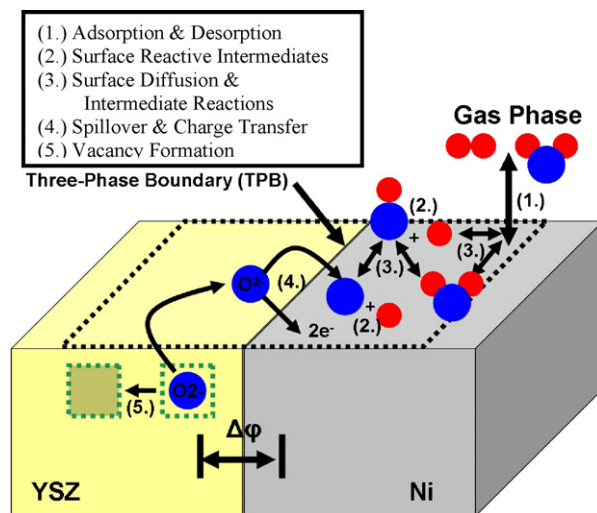|	
β	charge transfer coefficient, 0.5
γ	excess variable
ε	porosity
η	overpotential, V
θ_i	species surface coverage species $i = C_i/N_0$
ρ	density, kg m^{-3}
σ	conductivity, S cm^{-1}
φ	potential, V
ψ	scalar mass transfer coefficient $= L/D_{13}/C_T$

Superscripts

$\langle A \rangle$	area-specific
$\langle V \rangle$	volume-specific
0	initial or equilibrium value
g	gas phase
*	non-dimensional variable

Subscripts

i, j	species
V	surface vacancy

(1.) Adsorption & Desorption
(2.) Surface Reactive Intermediates
(3.) Surface Diffusion & Intermediate Reactions
(4.) Spillover & Charge Transfer
(5.) Vacancy Formation

Fig. 1. Schematic of the electrochemical mechanism considered in this work, adapted from [15,26]. The dissociative adsorption/desorption of $H_2^{(g)}$ and molecular adsorption/desorption of $H_2O^{(g)}$ (1) occurs on the Ni catalytic surface. Adsorption is limited to vacant surface sites. Adsorption is governed by the molecular impingement rates and statistical sticking coefficients of the respective molecules. All species are considered surface reactive intermediate species (2). These intermediates can diffuse on the Ni surface and propagate through a number of reaction pathways (3). Termination of the mechanism considers an interstitial O^{2-} maintains a spillover process from the bulk YSZ onto the Ni surface near the TPB (4). The O^{2-} looses two electrons and leaves a vacancy in the YSZ during the spillover process (5). The vacancy will be refilled by ionic transport. Because this represents a charge transfer process where the O^{2-} is being electrically neutralized by the electrochemical oxidation reaction as it spills onto the Ni surface, its rate is significantly affected by the local overpotential, which is of direct relation to the electrostatic potential difference ($\Delta\varphi$) across the Ni–YSZ interface.

the anode that is utilized for these reactions can be measured into the anode from the normal of the anode–electrolyte interface. For a porous Ni–YSZ cermet anode, recent use of discrete electrochemically active functional layers in high performance SOFC cells suggests that an active region of 5–20 μm can be expected [9,11–14].
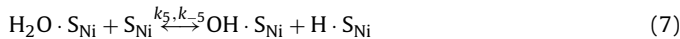
When percolation paths through the respective phases/regions to the TPB exist, electrochemical oxidation can occur. The Faradaic portion of this electrochemical process results in the consumption of hydrogen, production of water, and electrical neutralization of the ionic current in favor of an electronic current. The mechanism by which this process occurs can be represented by a series of competing chemical adsorption, desorption, and surface reactions [5,15–19]. Rate expressions associated with the mass flux of each of the participating species can be prescribed using a mechanistic description of these processes. In this work, localized and discrete boundary conditions are used to couple a representative kinetic mechanism describing these processes to a diffusion mass transport model. This coupling provides the ability to investigate the effects of the coupled electrochemistry and mass transport near the TPB regions of a SOFC anode. A lattice Boltzmann method (LBM) is used to describe the diffusion process. It is chosen because of its ability to treat complex pore geometries with a high fidelity while using a regular mesh/grid, localized porous microstructural effects, discrete and adaptive boundary conditions characteristic of electrochemical processes, and mass transport at micron to nanometer length-scales typical in a SOFC microstructure (i.e. a mean pore diameter of 0.1–1.0 μm). These requirements typically make more-traditional computational fluid dynamics (CFD) models based on the Navier–Stokes equations inaccurate or computationally.

The goal of this paper is to discuss the development of the tools necessary to examine the validity of a detailed and locally varying electrochemical boundary condition, coupled to a LBM scheme,

pathways to the current collector, electrolyte, and fuel channel, respectively. The region where the three discrete phases meet is typically described as the three-phase boundary (TPB). This region is noted in the schematic provided in Fig. 1, which is used in more detail in the proceeding sections. The charge/mass carriers, which take the form of the discrete Ni, YSZ, and pore-phases, exemplify the multifunctional nature of the problem. The resistivity of the YSZ to oxide ion transport is more substantial than the electronic resistivity of the Ni and the mobility of the H_2 fuel and H_2O product in the vapor phase. Therefore, the electrochemical oxidation reactions occur at TPB regions in the proximity of the anode–electrolyte interface [1,9,10]. These reactions occur in regions that are often characterized by an active utilization width. The active width of

for investigating mass transport in SOFC anode. This development is completed to provide a tool that is capable of providing a better understanding of the electrochemical and mass transport processes that occur in the TPB regions of the SOFC. A 2D, multi-species model is presented in this study. The extension of the numeric methods used to describe mass transfer in the SOFC structure to full 3D structures is straight-forward and documented elsewhere [20,21]. The use of actual SOFC microstructures for detailed quantitative characterization of the SOFC microstructure and/or as structural inputs which can consider the coupling of the electronic and ionic charge transport in the respective Ni and YSZ phases have recently been reported [21–25]. The inclusion of these details along with alternative electrochemical oxidation mechanisms will be considered in future studies. Some preliminary results are provided to demonstrate the capabilities of the approach and methods.

2. Method of approach

To provide a detailed and discrete understanding of the effects of the electrochemical oxidation mechanism, a detailed six-step reaction mechanism [15,16] is used to describe the details of the net oxidation reaction in Eq. (2). This mechanism represents a complete pathway and has been well discussed within the literature. There are several apparent shortcomings that will be discussed, but the mechanism provides a clean and detailed framework to understand the coupled system using the detailed kinetics. There has been a great deal of recent work in the formulation of a complete mechanism for the description of the electrochemical oxidation kinetics in the SOFC anode that provide their own unique merits, such as [17–19,26–28]. These mechanisms will be considered in future works that are focused on the detailed effects of the considered electrochemical mechanism from a more fundamental perspective. With this caution, the mechanism selected can be shown,

$$H_2^{(g)} + 2S_{Ni} \overset{k_1,k_{-1}}{\longleftrightarrow} 2H \cdot S_{Ni} \tag{3}$$

$$H_2O^{(g)} + S_{Ni} \overset{k_2,k_{-2}}{\longleftrightarrow} H_2O \cdot S_{Ni} \tag{4}$$

$$O \cdot S_{Ni} + H \cdot S_{Ni} \overset{k_3,k_{-3}}{\longleftrightarrow} OH \cdot S_{Ni} + S_{Ni} \tag{5}$$

$$H_2O \cdot S_{Ni} + O \cdot S_{Ni} \overset{k_4,k_{-4}}{\longleftrightarrow} 2OH \cdot S_{Ni} \tag{6}$$

$$H_2O \cdot S_{Ni} + S_{Ni} \overset{k_5,k_{-5}}{\longleftrightarrow} OH \cdot S_{Ni} + H \cdot S_{Ni} \tag{7}$$

$$O_O^x + S_{Ni} \overset{k_6,k_{-6}}{\longleftrightarrow} O \cdot S_{Ni} + V_{\ddot{O}} + 2e_{Ni}^- \tag{8}$$

where S_{Ni} is a Ni surface vacancy, $i \cdot S_{Ni}$ a Ni surface species intermediate, k_n and k_{-n} are the forward and reverse reaction rate constants for reaction n, respectively. An oxygen ion interstitial, O_O^x, and an oxygen ion vacancy, $V_{\ddot{O}}$, in the bulk YSZ are also used. A visual representation of the pathway is provided in the schematic shown in Fig. 1. Within this reaction mechanism, Eqs. (3 and 4) represent adsorption and desorption of the gas phase species onto the Ni surface, Eqs. (5–7) are surface intermediate reactions, and are consistent with Langmuir-Hinshelwood type kinetic processes, and Eq. (8) is the charge transfer reaction. All of the reactions in Eqs. (3–8) are considered reversible.

The mechanism described here maintains a number of important assumptions. These include: (i) the mechanism is derived for a pattern Ni–YSZ anode with discrete line phases of Ni and YSZ to control the TPB length, locations, and active widths. The mechanisms for a Ni–YSZ cermet anode are more complex and less understood; however, the requirement for the TPB condition is analogous. Further, (ii), Eq. (8) is the only charge transfer reaction and is considered as a two electron process. All other reactions are assumed to occur in a neutral manner and adsorption and desorption are non-activated reactions and therefore only dependent on local thermodynamic conditions. The charge transfer step, Eq. (8), (iii) is treated as a single elementary step derived from the oxygen

spillover onto the Ni surface. This results in a charge transfer mechanism that resembles that of the Butler–Volmer equation. Because hydrogen spillover onto the YSZ phase is not considered, (iv) the YSZ is not considered to be available as an active surface at this time. If these effects were considered, parallel and competing mechanisms on the respective Ni and YSZ surfaces could occur. Sufficient phases and continuous, or percolating, pathways are assumed for the respective charge carriers at active site boundary conditions; (v) concentrations of ion and ion vacancies are assumed constant in the electrolyte; (vi) reaction rate constants are assumed to be independent of surface coverage; (vii) intermediate surface species are bounded in such a way that no interaction with gas phase species occurs; (viii) hydrogen is adsorbed in a dissociative manner while water is adsorbed in molecularly. During this process, their associated initial sticking coefficients are assumed constant [29]; and (ix) the detailed carriers, pathways, and potentials associated with the electronic (Ni) and ionic (YSZ) charge carriers are neglected at this time.

Among the more significant assumptions made is that the overpotential in the TPB regions is assumed and held constant because the detailed charge carriers and pathways are neglected at this time. This work is intended to outline the development and coupling of the electrochemistry and diffusion processes, and therefore this discussion is limited to these processes. Since the initial development of these methods, additional papers that couple these charge transport processes with 1D effective medium model have been demonstrated by the authors [22]. Subsequent studies will incorporate these effects.

Despite the assumptions required to utilize the electrochemical mechanism, it is considered because it provides a complete mechanism with a strong basis for the necessary assumptions. Additionally, detailed sets of reaction rate constants were available from experimental work, surface science data available, and other analytic analysis [15,16]. More recent mechanisms consider the spillover of atomic hydrogen onto the YSZ surface and split the charge transfer process as single electron processes [19,26,28,30,31]. These works have shown improved replication of the cathodic branch of the Tafel plots when compared to experimental works and thermodynamic consistency for the Arrhenius behavior. These mechanisms will be considered in future works.

Understanding the limitations of the electrochemical mechanisms used in this study, the selection of a single rate-limiting step within the mechanism would permit the other rate equations to be equilibrated and a Langmuir–Hinshelwood type rate equation to be formed. However, several of the reactions within the mechanism may occur at similar rates and therefore a more rigorous analysis must be completed, which considers the rate change of surface intermediate species described in Eqs. (3–8). With these types of complex mechanisms, rate expressions for the surface intermediate species are formed through the completion of a species balance of the surface intermediates, as has been discussed in [15,16], providing:

$$\frac{\partial \theta_H}{\partial t} = \begin{pmatrix} 2k_1\theta_V{}^2 - 2k_{-1}\theta_H^2 - k_3\theta_H\theta_O \\ +k_{-3}\theta_{OH}\theta_V + k_5\theta_{H_2O}\theta_V - k_{-5}\theta_{OH}\theta_H \end{pmatrix} \tag{9}$$

$$\frac{\partial \theta_{H_2O}}{\partial t} = \begin{pmatrix} k_2\theta_V - k_{-2}\theta_{H_2O} - k_4\theta_{H_2O}\theta_O \\ +k_{-4}\theta_{OH}{}^2 - k_5\theta_{H_2O}\theta_V + k_{-5}\theta_{OH}\theta_H \end{pmatrix} \tag{10}$$

$$\frac{\partial \theta_{OH}}{\partial t} = \begin{pmatrix} k_3\theta_O\theta_H - k_{-3}\theta_{OH}\theta_V + 2k_4\theta_{H_2O}\theta_O \\ -2k_{-4}\theta_{OH}{}^2 + k_5\theta_{H_2O}\theta_V - k_{-5}\theta_{OH}\theta_H \end{pmatrix} \tag{11}$$

$$\frac{\partial \theta_O}{\partial t} = \begin{pmatrix} -k_3\theta_O\theta_H + k_{-3}\theta_{OH}\theta_V - k_4\theta_{H_2O}\theta_O \\ +k_{-4}\theta_{OH}{}^2 + k_6\theta_V + k_{-6}\theta_O \end{pmatrix} \tag{12}$$

$$1 = \theta_V + \theta_H + \theta_{OH} + \theta_{H_2O} + \theta_O \tag{13}$$

Table 1
Kinetic reaction rate constants at 973 K from Bessler [16].

	k_1	k_2	k_3	k_4	k_5
k_{+n} [s^{-1}]	x	x	2.0×10^{11}	1.0×10^{12}	6.0×10^{5}
k_{-n} [s^{-1}]	2.4×10^{8}	1.0×10^{11}	1.3×10^{4}	5.8×10^{2}	1.5×10^{0}

In these equations t is time, θ_i is a non-dimensional surface coverage of a surface intermediate species which represents the fraction of available surface sites covered by that surface species, and V denotes the Ni surface vacancy coverage. As shown, the gas phase surface concentration of hydrogen and water are incorporated into k_1 and k_2 as partial pressures, respectively. The YSZ oxygen vacancies and ion concentrations are used for the treatment of k_6 and k_{-6}, respectively. It is assumed that these concentrations do not appreciably deviate from equilibrium during oxidation to perform this elimination. A total site balance, shown in Eq. (13), effectively closes the set of first order differential equations in Eqs. (9–12).

Values for the reaction rate constants from Bessler [16] are shown in Table 1. These reaction rate constants were chosen because they are based upon surface measurements and optimized to fit by means of electrical impedance spectroscopy (EIS) to experimental data. It should be noted that k_1, k_2, k_6, and k_{-6} all require individual treatment to model the physical systems. Additionally, the rate constants can generally be adjusted for temperature through an Arrhenius relationship; however, there are some thermodynamic inconsistencies in the formulation that make use of the temperature dependence intractable at this time [32]. Thermodynamic consistency and closure is met with more recently proposed mechanisms that will be considered in future studies.

The reaction rate constants k_1 and k_2 require custom treatment for this study. These rate constants are associated to the adsorption of gas phase hydrogen and water. Thus, they also are responsible for the coupling the electrochemical kinetics to the LBM diffusion processes. From kinetic theory, a rate of impingement of particles of species, i, is defined as,

$$I_i = \frac{P_i}{\sqrt{2\pi \cdot m_i \cdot k_{\mathrm{b}} \cdot T}} \tag{14}$$

where P_i is the partial pressure of species, i, at the location of impingement, m_i is the mass, k_{b} is Boltzmann's constant, and T is the absolute temperature.

Using Eq. (14), the rate constants for the adsorption of gas phase hydrogen and water onto the Ni surface, found in the reactions in Eqs. (2 and 3), can be formed. A simplified form of the expressions for k_1 and k_2, for hydrogen and water, respectively, is found as,

$$k_1, k_2 = 2.6 \cdot 10^{24} \frac{P_i}{\sqrt{M_i \cdot T}} \cdot \frac{s_i^0}{N_0} \tag{15}$$

where M_i is the molecular weight, s_i^0 is the initial sticking coefficient for species i, and N_0 is the total number of active sites.

Like k_1 and k_2 limit the rate of adsorption of hydrogen and water, k_6 and k_{-6} bound the Faradaic charge transfer process. Completing a charge balance for the forward and reverse directions of Eq. (8), the charge transfer rate constants are derived,

$$k_6 = k_6^0 \cdot \exp\left(\beta \frac{nF}{RT}\eta\right) \tag{16}$$

$$k_{-6} = k_{-6}^0 \cdot \exp\left(-(1-\beta)\frac{nF}{RT}\eta\right) \tag{17}$$

where η is the overpotential, β is the charge transfer coefficient, R is the universal gas constant, F is Faraday's constant, n is the number of electrons per hydrogen (i.e. 2), and k_6^0 and k_{-6}^0 are the equilibrium reaction rate constant at zero overpotential.

The area-specific Faradaic current density in W m^{-2}, $i_F^{\langle A \rangle}$, resulting from the reaction is,

$$i_F^{\langle A \rangle} = 2F \frac{N_0}{N_{\mathrm{A}}}(k_6 \theta_V - k_{-6}\theta_0) \tag{18}$$

where the number density of available surface sites, N_0, and Avogadro's number, N_{A}, are required properties. This differs from the volume-specific Faradaic current density in W m^{-3}, $i_F^{\langle V \rangle}$, which is normalized by the length of the computational domain, L. Both versions of the Faradaic current density are necessary at this time. This is because the reactions occur at a discrete interface, requiring an area-specific current density for treatment of the molar fluxes resulting from the Faradaic processes in the mass transfer model. Conversely, because the electronic and ionic charge carriers are not explicitly treated at this time in this study, the volume-specific Faradaic current density is required. The volume-specific current density is used to determine the local electronic and ionic current densities using a simple charge and mass balance. In Eq. (18), there should be zero net current density at zero overpotential, as this implies equilibrium. Separating terms in Eq. (18), two individual terms can be derived that must individually be equal to a constant reference current density. Rearranging, equilibrium rate constants k_6^0 and k_{-6}^0 are derived,

$$k_6^0 = \frac{N_{\mathrm{A}} \cdot i_0}{2F \cdot N_0 \cdot \theta_V^0} \tag{19}$$

$$k_{-6}^0 = \frac{N_A \cdot i_0}{2F \cdot N_0 \cdot \theta_0^0} \tag{20}$$

where θ_i^0 is the equilibrium coverage at zero overpotential for species i, and i_0 denotes the reference exchange current density. This equilibrium coverage can be calculated by solving the system of differential equations in Eqs. (9–12) with k_6^0 and k_{-6}^0 set to zero.

The mechanisms is now completely defined and the molar hydrogen flux is found using Faraday's law,

$$\overrightarrow{J_{\mathrm{H_2}}} \cdot \vec{n} = -\overrightarrow{J_{\mathrm{H_2O}}} \cdot \vec{n} = \frac{i_F^{\langle A \rangle}}{2F} \tag{21}$$

where $\overrightarrow{J_{\mathrm{H_2}}}$ is the hydrogen flux, $\overrightarrow{J_{\mathrm{H_2O}}}$ is the water flux, and $\vec{n}$ is the unit normal.

At this point, the electrochemical system is defined in terms of localized partial pressures, overpotentials, and other inputs characteristic of the SOFC active region. In accordance with Eq. (21), the flux defined by the electrochemical model must occur in a direction normal to the active surface.

To couple the electrochemical mechanism to the LBM scheme, electrochemically active flux boundary conditions are defined. These boundary conditions are placed at any local boundary node in the computational domain. Conceptually, the treatment of the active boundaries within the computational domain is shown in Fig. 2. The geometric input file for the LBM is a binary representation of the structure, where '0' represents an impermeable dense phase (i.e. Ni or YSZ) and '1' is the pore-phase. With the updated scheme, to prescribe an *interface* as electrochemically active, a '2' is used to designate the local LBM node as requiring a discrete and local analysis of the electrochemical kinetics. More complete details on the origin of the binary geometric representation and the application to real geometric structures are described elsewhere [33].

To treat the electrochemical kinetics with this type of representation, the reaction rate constants k_1, k_2, k_6, and k_{-6} are all updated at each active boundary location based upon the localized surface partial pressures and overpotential. The system of differential equations, Eqs. (9–12), is solved to steady state at each active boundary point for each time step in the mass transfer solution. This type of solution method is required, with updated rate constants,
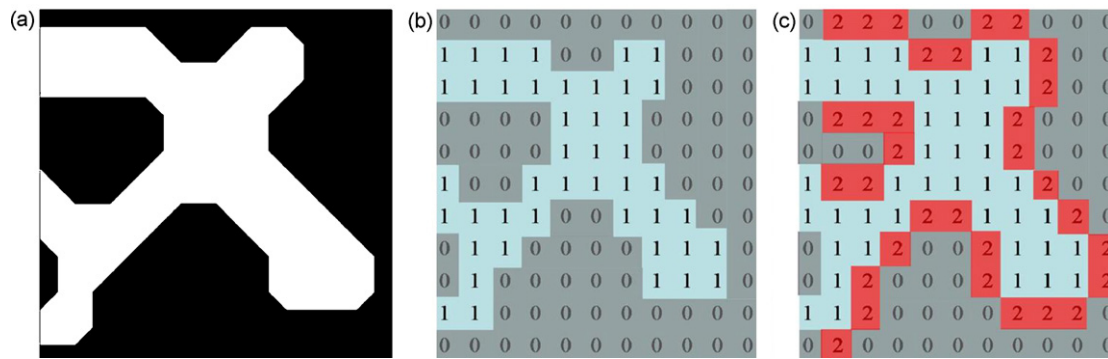
Fig. 2. A conceptual representation of the implementation of geometric structures into the model. (a) A representation of the pore-structure where the white regions are the pore and the black regions represent the dense Ni and YSZ materials. (b) A binary representation of this structure, as is read by the LBM, where '1' is a pore and '0' is a dense region. (c) Discrete electrochemical boundary conditions are implemented with a unique binary indicator, '2', at the interface. False colors are used as a visual guide.

for every LBM iteration step and is permissible using the pseudo-steady state approximation (PSSA). The PSSA assumes that the residence time of the surface intermediate species, also called reactive intermediates, is much smaller than any characteristic time of the transport processes as is a common assumption in catalytically assisted reaction kinetics [32,34]. Residence times for these catalytic reactions are typically on the order of pico- to nano-seconds. Because of the differences in time scales, the system of differential Eqs. (9–12) is a stiff system of equations. A fourth-order Rosenbrock method is used to facilitate rapid convergence. Analysis of the transient solutions provides equilibration on the order of a nanosecond and provides further confidence in the use of the PSSA steady state solutions for the LBM mass transfer model. Similar approximations and estimations have been made using impedance data [15,16,35].

The LBM used for the diffusion model in this study is based on the two-species LBM originally proposed by Luo and Girimaji [36] and extended by McCracken and Abraham for species of different molecular weights [37]. The approach used here is consistent with that of Joshi et al. who demonstrated the extension of this approach for more than two-species with different molecular weights [38] and non-continuum diffusion [39]. Fluxes applied by the LBM are calculated for each surface normal as described by Shan and Doolen [40]. Fluxes from concave boundaries are not considered (see Appendix B). Computational domain inlet mole fractions are fixed. Bounce-back, or zero slip, boundary conditions were used on any solid surface that is not prescribed with a flux or as an electrochemically active node [38,41]. Consistent with the conservation principles, density, concentration, component velocity, and mass average velocities are tracked and used throughout the computational domain. Additional details on the numeric methods employed in the LBM diffusion models are available in Appendix A, which reviews methods developed in other publications [20,33,38,39]. Appendix B provides more mathematical details with regard to the development and implementation of the discrete electrochemical kinetic boundary conditions within the LBM algorithm.

Physically, the LBM mass transport model assumes continuum diffusion. Computational models were developed using FORTRAN. Parallelization was completed using Message Parsing Interface (MPI) routines with an Intel compiler on a SGI Altix 3700. The use of LBM provides a scalable computational framework through vertical decomposition schemes.

3. Results and discussion

3.1. Model verification

To verify the implementation of the electrochemical reaction kinetics, their coupled use with the LBM mass transport model requires verification. The LBM mass transfer model has previously been reported by the authors. These studies include the detailed multi-component mass transfer verifications and validations using a variety of analytic and numeric techniques. Further, the LBM algorithm has been show to recover Navier–Stokes formalism and the corresponding species, and mass conservations properties [20,33,38,39]. Detailed verifications are not repeated here.

The implementation of the electrochemical reaction kinetics is initially verified independently of the LBM mass transfer model. This is performed by comparing the individual species' surface coverage as a function of the overpotential. The model predictions for these surface coverage values are compared to those that have been previously reported within the literature [16]. This verification is completed at 973 K, 101.325×10^3 N m^{-2}, 10^{19} sites m^{-2} Ni catalytic site density, 0.4 and 1.0 H_2 and H_2O vapor initial sticking coefficients, respectively, 420 A m^{-2} exchange current density, and partial pressures of hydrogen and water at 2.5×10^4 N m^{-2} and 40 N m^{-2}, respectively. Results from this successful verification of the model are provided in Fig. 3.

To elaborate further upon the physical behavior observed in Fig. 3, the effect of Faradaic reaction on the overall electrochemical processes is also observed. At zero overpotential there is no means to drive the surface reactions so the system is primarily composed
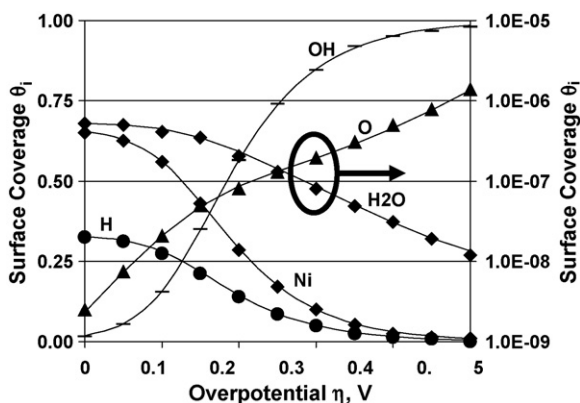
Fig. 3. Verification of the electrochemical kinetic mechanism's implementation using predicted reactive intermediate surface species coverage, θ_i, versus applied overpotential, η, at 973 K, 101325 N m^{-2} total pressure, and partial pressures of H_2 and H_2O of 2.5×10^4 and 4×10^1 N m^{-2}, respectively, 420 A m^{-2} exchange current density, and 1.67×10^{-5} mol m^{-2} Ni active surface site density. Results are compared to those reported in the literature, where the lines are values predicted by the electrochemical model in this study and the symbols are values interpreted from Bessler [16].

of vacancies and hydrogen intermediates. The surface coverage of hydrogen at zero overpotential is a function of the hydrogen partial pressure, or mole fraction. At this equilibrium, there is no charge transfer to facilitate the development of oxygen that promotes other surface intermediates. The oxygen surface coverage increases with increasing overpotential, facilitating the surface reactions and increases the coverage of the hydroxide intermediate. The increases of oxygen and hydroxide intermediates occupy active sites that were previously vacant or contained hydrogen. As the overpotential is further increased, the system begins to saturate with hydroxide around 400 mV. Around this point, there is no longer sufficient hydrogen or vacancies available. Also shown in Fig. 3, water plays only a minor role in the surface reactions. However, it does still play a significant role in the partial pressure of hydrogen and therefore is important when the electrochemical system is coupled to the diffusion processes.

3.2. Coupled electrochemical and mass transfer model

With the independent validation of the electrochemical and LBM diffusion models completed, the models are combined for more detailed studies. However, the non-dimensional molar flux definition is required for the combined system. Previous efforts have considered a constant non-dimensional flux, J^*, for a tertiary system,

$$J^* = \frac{J \cdot L}{C_T \cdot D_{13}} \tag{22}$$

where the non-dimensional flux is used to scale the LBM results with the real, physical problem [38]. In Eq. (22), J is magnitude of the flux vector, L is the domain length, C_T is the total concentration, and D_{13} is molecular diffusivity for species 1 and 3 (H_2 and N_2, typ.). This is replaced by D_{12} for a binary system. However, when the electrochemical kinetics is combined with the LBM mass transfer model, the electrochemically active interfaces maintain discrete fluxes, which are dependent upon the local properties and conditions. As a result, the mass non-dimensional molar flux is defined locally for each flux calculated by the electrochemistry model such that:

$$J^*(x,y) = \frac{\bar{J}(x,y) \cdot L}{C_T \cdot D_{13}} = \psi \cdot \bar{J}(x,y) \tag{23}$$

where $\bar{J}(x,y)$ is the local molar flux vector. Due to the addition of the electrochemical model, the average molar flux is no longer a stand-along input parameter. Rather, the fluxes vary with the local H_2 and H_2O partial pressures and overpotential. In a secondary manner, local H_2 and H_2O partial pressures are directly related to extensive model properties such as the domain size, total concentration, and diffusivity. Therefore, results will be discussed in terms of the scalar flux coefficient, $\psi = (L/C_T/D_{13})$, and the overpotential, η. The scalar flux coefficient, ψ, represents the resistivity and size of the domain with respect to mass transfer. These terms are not sufficient to describe the entire system, but do quantify important system parameters in a manner suitable for consistent evaluation irrespective of their individual values. It additionally allows for the comparison and treatment in a manner similar to classical continuum mass transport and previous publications.

To better understand the coupled system and verify its implementation, a simple 2D channel is considered. This geometry, which could be representative of a single straight pore, is shown in Fig. 4. A constant mole fraction is specified at the inlet ($x = 0$) and electrochemically active surfaces are set at $x = L$. Both the active surface and inlet run the entire height of the fluid domain ($y = 0–H$). Bounce-back, or zero diffusive flux, boundary conditions are applied on the walls at $y = 0$ and $y = H$. Electrochemical reactions occur only at the active surface.
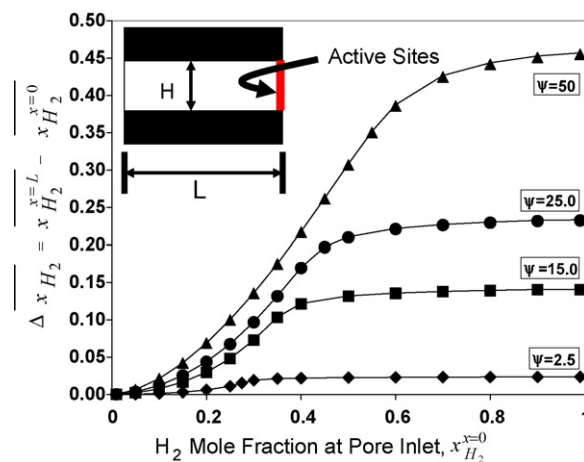

Fig. 4. A 2D pore of length, L, is used for the examination of the coupled electrochemical and mass transfer processes. Impermeable solid boundaries are placed at a height, H, apart, electrochemically active boundaries are placed along the right-hand pore outlet, and hydrogen and water mole fractions are applied at the adjacent pore inlet. The non-dimensional flux coefficient, $\psi = L/C_T/D_{12}$, and thus the non-dimensional flux, J^*, and inlet H_2 mole fraction were parameterized for this study. At lower ψ values and higher inlet H_2 mole fractions, the problem is kinetically limited. However, as ψ increases and/or the inlet H_2 mole fraction decreases, concentration losses begin to take hold. Because a constant overpotential is considered, the onset of concentration losses begins to slow the Faradaic conversion of H_2 to H_2O at the active boundary. The red boundary line is provided to guide the eye and was defined using Fick's law with the Faradaic flux determined for each solution at the active boundary.

For this geometry, the detailed electrochemical kinetics is coupled with the LBM mass transfer model, which is allowed to equilibrate based upon the applied overpotential, scalar flux coefficient, ψ, and the applied boundary conditions. In this study, a conceptual mixture of H_2 and H_2O is considered and the inlet mole fractions are varied for constant scalar flux coefficients. This LBM model is then compared to mass transfer calculated using 1D Fick's law, which is represented by the solid lines in Fig. 4. The Fick's law calculations are obtained by using the averaged molar flux calculated by the electrochemical portion of the coupled LBM model once the solution is converged. The agreement for the two systems provides verification of the implementation. A 500 mV overpotential is consistently used so that the effects of ψ can be understood in more detail. The results presented in Fig. 4 are plotted as a change in H_2 mole fraction from the pore inlet to the active wall. This difference is plotted versus the H_2 mole fraction at the pore inlet.

There are several significant observations that can be made concerning the results provided in Fig. 4. It is first noted that when sufficient H_2 is present, there is a change in H_2 mole fraction within the channel that follows an asymptotic trend (e.g. $\Delta \overline{x_{H_2}} \to$ const.). This occurs because there is sufficient H_2 at the active boundary to consistently propagate through the electrochemical oxidation reactions in this regime. The ability for a sufficient H_2 supply at this boundary is both a function of its inlet concentration as well as the scalar flux coefficient, ψ, which describes the effective mass transfer resistivity and size of the domain. However, as the inlet H_2 mole fractions are decreased and/or the scalar flux coefficient, ψ, is increased, the active boundaries begin to become starved of H_2 and the electrochemical reaction rates slow. In this instance, there is no longer sufficient H_2 available for adsorption and subsequent electrochemical reactions; this results in the electrochemical model being rate-limiting. As seen in Fig. 4, the change in H_2 mole fraction approaches zero as concentration losses dominate the system. The region between these two limits is a region where both the mass transfer and the electrochemical surface reactions are significant. This ability to capture both the mass transfer and
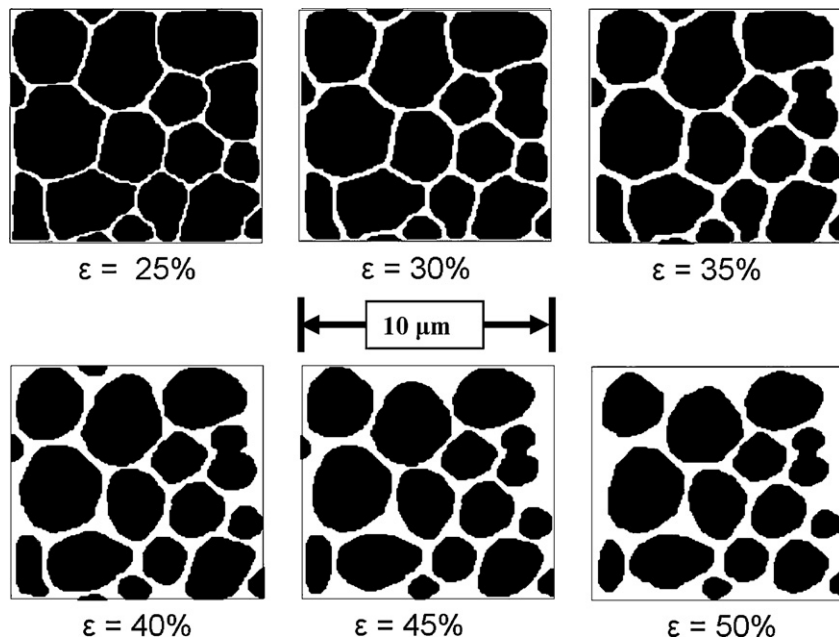
Fig. 5. Six phenomenological structures were considered in this study. These structures, from [33], are comprised from the same initial structure and maintain porosities ranging from 25% to 50%. The geometric files are comprised of 151×151 lattice points. These structures are considered as a $10\,\mu m \times 10\,\mu m$ section of the anode interlayer for all analyses performed in this study.

electrochemical limitations is critical for understanding fuel cell operation.

3.3. Coupled electrochemical kinetics and mass transfer in conceptual SOFC interlayer

With a preliminary understanding of the coupled LBM and electrochemical kinetics model, it is pertinent to apply them to a representative system to better understand their effect. To pursue such an effort, we consider six conceptual structures, which are shown in Fig. 5. These structures have previously been used to demonstrate the coupled effect between porosity and flux (i.e. current density) on concentration losses for a typical SOFC anode [33]. Here, we perform a more detailed investigation. At this time, these structures are treated as being representative of a $10\,\mu m$ electrochemically active interlayer in a SOFC anode. The solid/pore interfaces are treated as being electrochemically active. We consider $x = 0\,\mu m$ as being the anode support/interlayer interface and $x = 10\,\mu m$ as the anode interlayer/electrolyte interface. We refer to the x-direction (i.e. left to right) as the primary transport direction and the transverse y-direction (i.e. top to bottom) as the spanwise direction. In this study, all local fluxes in the LBM model are described using Eq. (23) and are scaled using a non-dimensional

electrochemical parameter A^*,

$$A_* = (L_{\text{TPB}} \cdot w_{\text{active}} \cdot L_{\text{RVE}})_{\text{RVE–Phys.}}$$

$$= A_{\text{coef}}\left(N_{\text{active}} \cdot A_{\text{LU}} \cdot \frac{N_x}{N_x N_z N_z}\right)_{\text{RVE–LBM}} \tag{24}$$

which accounts for the number of electrochemically active nodes in the LBM model, and scales that area with an input three-phase-boundary length, L_{TPB} in m^{-2}, active width from the TPB, w_{active} in m, and the Representative Volume Element (RVE) length, L_{RVE} in m. Again, the RVE length is set as the entire $10\,\mu m$ interlayer. In Eq. (24), A_{coef} is a calculated scaling parameter that is used in the LBM model to ensure A^* maintains an appropriate magnitude. While the TPB length and electrochemically active width can be parameterized using detailed characterizations and/or approaches like percolation theory, they were held constant in this study [42–45]. This was purposely done so the effects of the porosity, overpotential, and kinetics could be verified, understood, and explored in detail. The properties considered in this study are provided in Table 2, which includes references that were used to estimate the appropriate magnitude of these parameters.

A key assumption made in the present study is that a constant overpotential, η, is applied to the entire interlayer. It is treated as

Table 2
Thermodynamic and structural properties considered for parametric study.

Property	Value	Notes and references
Porosity, ε	$25\% \rightarrow 50\%$	Parameterized
Overpotential, η	$10 \rightarrow 500\,\text{mV}$	Parameterized [3,16]
TPB length, L_{TPB}	$3 \times 10^{13}\,\text{m}^{-2}$	[23–25,46]
Active width, w_{active}	$20\,\text{nm}$	[26,28,46]
Representative volume length, L_{RVE}	$10\,\mu\text{m}$	Interlayer [1,3,14,46]
Temperature, T	$973,\text{K}$	[3,6,14,16]
Total pressure, P_{T}	$101.325,\text{kPa}$	[3,6,14,16]
Total concentration, C_{T}	$12.525,\text{mol\,m}^{-3}$	Ideal gas law
Diffusivities, $\left[D_{\text{H}_2,\text{H}_2\text{O}}, D_{\text{H}_2,\text{N}_2}, D_{\text{N}_2,\text{H}_2\text{O}}\right]$	$[6.65, 5.44, 1.91]$, $\text{cm}^2\,\text{s}^{-1}$	Chapman-Enskog [48]
Equilibrium mole fractions $\left[x_{\text{H}_2}^{\text{Eq.}}, x_{\text{H}_2\text{O}}^{\text{Eq.}}, x_{\text{N}_2}^{\text{Eq.}}\right]$	$[0.500, 0.200, 0.300]$	Assumed
Active region mole fraction $\left[x_{\text{H}_2}^0, x_{\text{H}_2\text{O}}^0, x_{\text{N}_2}^0\right]$	$[0.333, 0.333, 0.334]$	Assumed
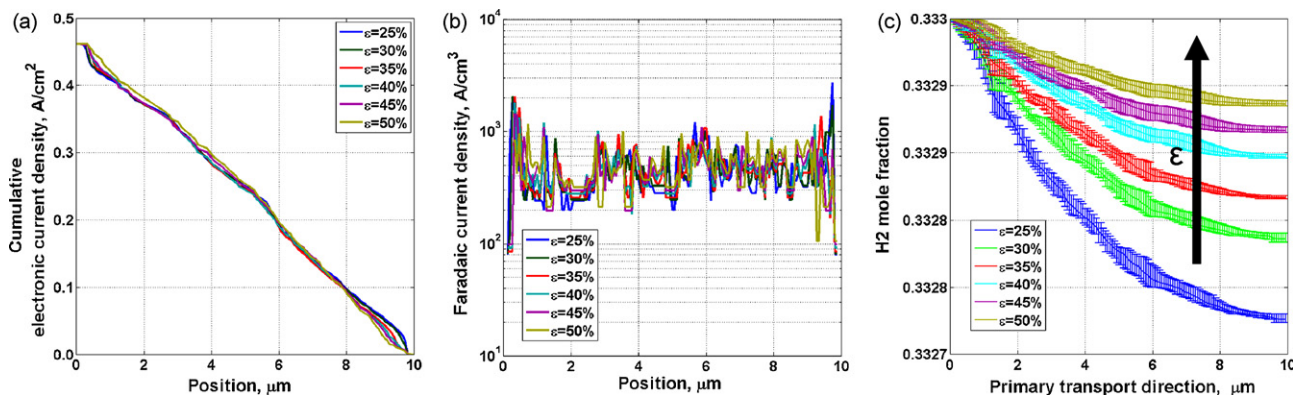
Fig. 6. (a) The local electronic current density, i_{el}, resulting from the Faradaic portion of the electrochemical oxidation kinetics are shown as a function of position within the 10 μm active region is shown, for a 200 mV overpotential. Trends for six conceptual structures with a porosity ranging from 25% to 50% are shown. Similarly (b) provides the net volume-specific Faradaic current density as a function of position for the same cases. Finally, (c) provides the mean H_2 mole fractions along the primary transport direction (left to right in the x-direction) with the span-wise variations (y-direction) represented with scatter-bars. The direction of increasing porosity is noted with an arrow. Additional parameters used for this study are provided in Table 2.

an independent input parameter. This is undoubtedly an approximation that has substantial impact on the local fluxes predicted by the electrochemical kinetics models. Because the overpotential is related to the local difference in electronic and ionic potentials, the large ionic resistivity of the YSZ phase will undoubtedly force a non-linear Faradaic current density with larger overpotentials near the anode/electrolyte interface where the ionic current density is larger and yet-to-be electrochemically neutralized. Detailed descriptions of the electronic and ionic charge carriers are necessary to capture these effects, some preliminary efforts by the authors to account for these details have been reported and will be explored in more detail in future studies [22]. Several other groups have also captured these types of details with unique computational approaches [13,26,30,46,47].

With an understanding of the implication of the assumptions used in the present model, a parametric study is performed. Beginning with Fig. 6, the electronic current density, which is defined as a function of the position along the primary transport direction, can be interpreted through the integration the volume-specific Faradaic current density along the primary transport direction,

$$i_{el}(x) = i_{el}^0(x = L) - \int_{x=L}^{x} \left[\frac{1}{H} \int_{y=0}^{y=H} i_F^{\langle v \rangle}(x, y) \cdot dy \right] \cdot dx \qquad (25)$$

where it is averaged over the transverse, or span-wise, direction through an initial integration. In Eq. (25), $i_{el}^0(x = L)$, is consistently defined as zero in this study, representing the anode/electrolyte interface. If a region away from this interface were considered, it could be set to a constant value. This would necessitate fluxes being specified at nodes along this boundary according to Faraday's law. This would be treated in a manner that is consistent with methods that have already been reported [33,38,39]. Also in Fig. 6, the volume-specific Faradaic current density, and H_2 mole fraction variations are shown for the six phenomenological structures shown at a 200 mV overpotential, with the properties provided in Table 2. In Fig. 6, several interesting observations can be made. First, Fig. 6a, shows that the electronic current density is rather consistent for all six structures considered. As expected, it is zero at $x = 10$ μm, which represents the anode/electrolyte interface. It increases rather linearly from $x = 10$ μm to $x = 0$ μm, as is confirmed by a rather flat spectrum of the Faradaic current density for all of the structures in Fig. 6b. The consistency in the electronic current density and the Faradaic current density is the result of several factors. First, without a parallel description of the charge transfer processes and consistent electrochemical structural properties (i.e.

L_{TPB} and w_{active}), the porosity does not influence these properties as would be expected. This observation suggests that these effects will need to be captured in future studies and should have a key impact on how the system behaves in trying to replicate the actual SOFC behavior. However, this result also provides a qualitative validation to the coupled model. As observed in Fig. 6c, the active region inlet mole fractions were also held consistent, irrespective of the geometry being considered. Because small variations in H_2 mole fraction are observed for all of the studies performed, this result is not only expected but also provides a verification of consistent implementation for all of the considered structures. Comparing to the observations in made with respect to Fig. 4, this effect is analogous to a region where a constant scalar flux coefficient, ψ, is considered (e.g. between the systems), and there is sufficient H_2 that the kinetics is not concentration limited. Despite the rather consistent Faradaic current densities noted in Fig. 6, Fig. 6c demonstrates the effect that the porosity has on the mass transfer processes. In Fig. 6c, the mean H_2 mole fraction along the primary transport direction is provided for each structure. The scatter-bars represent the span-wise variation in mole fraction (i.e. along the y-direction). While the absolute changes in H_2 mole fraction are small due to the small geometric size, the changes in the H_2 gradient substantially vary with decreasing porosity. Further, we expect larger H_2 mole fraction variation when a parallel description of the charge transfer processes and consistent electrochemical structural properties are considered due to their dependence on coupled geometric, transport, and kinetic properties.

Because the structure with a porosity of 25% maintained the largest mole fraction gradients at a 200 mV overpotential, Fig. 7 takes a closer look at this result. In Fig. 7, the scalar distributions of the H_2, H_2O, and N_2 mole fractions are shown in Fig. 7a–c, respectively. As expected, H_2 is consumed while H_2O is generated in the primary (x) transport direction. Interestingly, N_2 also varies along the primary transport direction with the reason given below. Fig. 7d provides the mean mole fractions along the primary transport direction with the scatter-bars representing the span-wise variation for this study. Recasting these results with the use of a non-dimensional excess variable similar to those used in radiation heat transfer, Fig. 7e provides a consistent non-dimensional representation of these results. The non-dimensional excess variable for H_2,

$$\gamma_{H_2}(x) = 100\% \cdot \frac{\overline{x_{H_2}}(x) - x_{H_2}^{min}}{x_{H_2}^{max} - x_{H_2}^{min}} \qquad (26)$$

where the maximum and minimum mole fractions can be defined anywhere in the domain and similar forms can be shown for H_2O
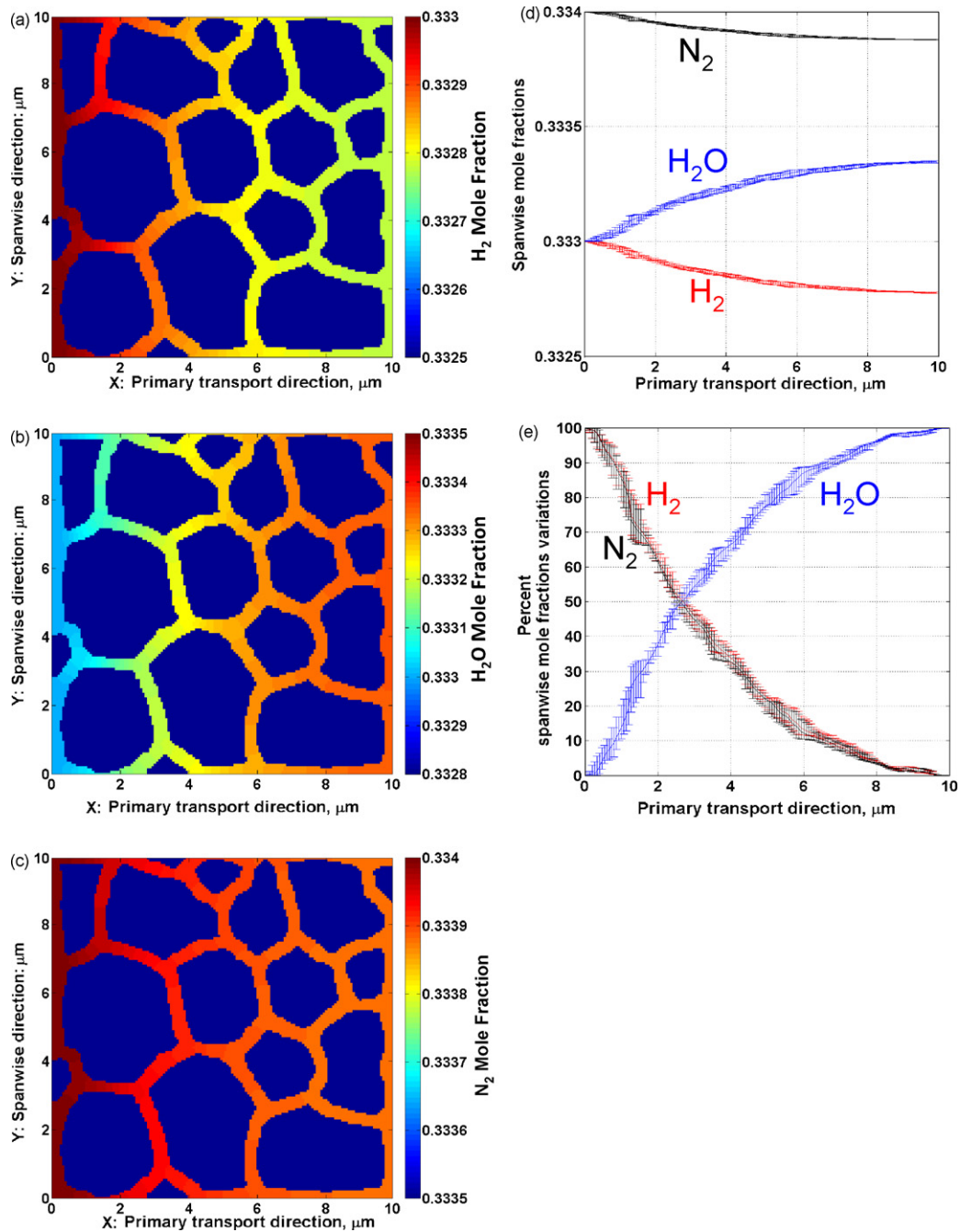
Fig. 7. The LBM mass transport and electrochemical kinetics model is used to study the effect of the 25% porosity structure on mass transport at $\eta = 200$ mV overpotential. The local (a) H_2, (b) H_2O, and (c) N_2 mole fractions are presented. (d) The average mole fractions along the primary transport direction (x-direction) with the scatter-bars representing the maximum and minimum span-wise (y-direction) variation. (e) The result is recast as an excess variable, Eq. (26) describing the localized percent variation.

and N_2. In Fig. 7e, the electrochemically inert N_2 follows the H_2 trend due to the larger molecular weight H_2O trying to diffuse out of the system and is consistent with traditional Stefan–Maxwell transport theory [48].

With a detailed understanding of the effect of the porosity on the coupled kinetics and transport processes, the applied overpotential is varied for the structures maintaining a porosity of 25%, 35%, and 45%, respectively. Overpotentials of $\eta = 10$, 100, 200, 300, 400, and 500 mV are considered for each of these structures, again using the properties reported in Table 2. The results of this study are presented in Fig. 8, where the electronic current density and H_2 mole fraction variation is reported in the three structures, respectively, for each considered overpotential.

In Fig. 8a, the cumulative electronic current density increases with increasing overpotential, which is noted by the arrow. While not visible in this figure, the 10 mV overpotential actually shows a negative electronic and Faradaic current density near $x = 10$ μm and thus a net production of H_2 from H_2O. The reason for unusual result is that while a consistent interlayer mole fraction is prescribed in all of the discussed studies, an equilibrium mole fraction is necessary for describing the equilibrium surface coverage values in the electrochemical kinetics model. Naturally, in a whole cell, this should be the value at the fuel channel inlet under open circuit conditions. To this effect, Table 2 notes the mole fractions prescribed at the fuel channel. In an actual system the inlet at the anode support/interlayer interface would be dictated by the operational
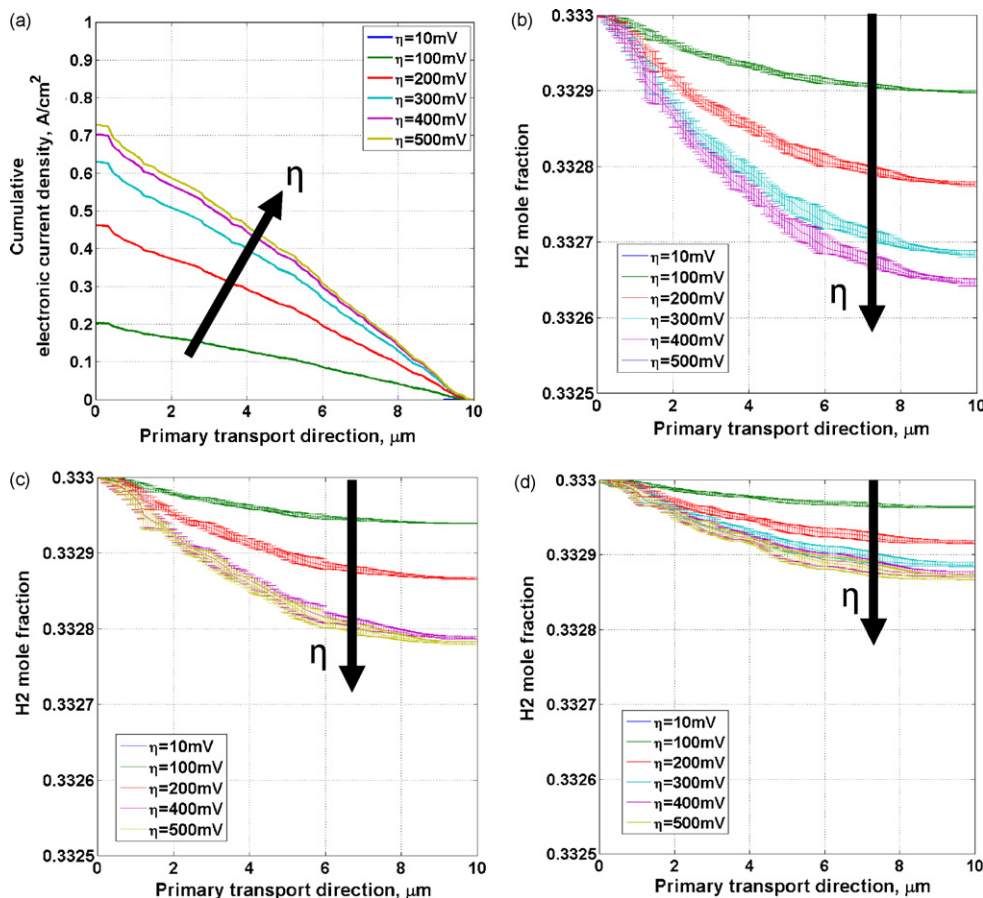
Fig. 8. (a) The characteristic electronic current density resulting from the Faradaic electrochemical processes within the considered structures as a function of the overpotential, η. The local variations in H_2 mole with increasing overpotential for the geometric structures maintaining a porosity, ε, of (b) 25%, (c) 35%, and (d) 45% are shown as a function of the position along the primary transport direction (x-direction). The average H_2 mole fractions are shown for the three geometries, respectively, with the scatter-bars representing the maximum and minimum mole fractions observed in the span-wise direction (y-direction). The thermodynamic and structural properties and conditions used are provided in Table 2. The arrows indicate the direction of increasing overpotential in each of the sub-figures.

conditions, structure, etc. In this study the channel equilibrium and interlayer inlet were fixed and a gradient was present. At a low overpotential, this difference in equilibrium and inlet mole fractions resulted in the cathodic branch of the electrochemical kinetics to overtake the anodic ones and the numeric model predicted an electrolysis-type condition. This suggests the importance of coupling the model with more-general cell-level models for the prediction of boundary conditions at the RVE level for future studies. While the present case is an artifact, it demonstrates the detailed predictive capability of the approach.

Returning to Fig. 8a, at a higher overpotential, the cumulative electronic current density begins to approach an asymptote. Undoubtedly, this is linked to the surface kinetics in the electrochemically model saturating with an OH^- surface species and being unable to support further electrochemical oxidation. Moving to Fig. 8b–d, increasing H_2 mole fraction gradients occur with increased overpotential and/or decreased porosity. Again, mean values along the primary transport direction are reported for the structures with (Fig. 8b) 25%, (Fig. 8c) 35%, and (Fig. 8d) 45% porosity. Scatter-bars represent the maximum and minimum span-wise variations in mole fraction and arrows are used to indicate the direction of increasing overpotential. The dependence on porosity and overpotential is noted, where the variations in H_2 mole fraction follow $\varepsilon = 45\% < 35\% < 25\%$ for each overpotential, η, due to changes in the area available for transport. However, further investigation of the impact of a correlation between the porosity (i.e. or phase volume fraction), respective cross-sections for the charge transfer

processes, and the electrochemically active area will be necessary in future studies to better understand these effects.

The final study considered for this work is an examination of the effect of the onset of concentration limited reaction kinetics. To explore these effects, the H_2 mole fraction at the interlayer inlet (i.e. $x = 0$), is set from a values consistent with Table 2 ($x_{H_2}^0 = 0.333$), to a value approaching zero ($x_{H_2}^0 = 0.001$). The interlayer inlet H_2O mole fraction is varied to compensate for the changes in H_2 mole fraction and the N_2 mole fractions is held consistently at 0.334 at the inlet. The equilibrium mole fractions at the channel remain consistent with those reported in Table 2. An overpotential of $\eta = 400$ mV is set and the same structures that were used in Fig. 8 are used.

The effect of the decreased H_2 concentrations has on the coupled kinetics and mass transfer processes are shown in Fig. 9. In Fig. 9a, the electronic current density resulting from the Faradaic processes is shown in the structure maintaining a 25% porosity for interlayer inlet H_2 mole fractions of ($x_{H_2}^0 = 0.001$–0.333). As the inlet H_2 mole fraction continues to increases, the kinetics becomes relatively consistent. However, at lower inlet H_2 mole fractions, the kinetics are impeded by the reduced H_2 concentration and the Faradaic consumption of H_2 is reduced. It is important to note that these studies are performed at constant overpotential, and therefore concentration losses translate into a reduction being observed in the Faradaic processes. As the inlet H_2 mole fraction approaches $x_{H_2}^0 = 0.100$ and above, consistent results are observed as mass transfer effects no longer have a prominent effect in the oxidation kinetics (i.e. there is sufficient H_2 available). Similar trends can be shown for
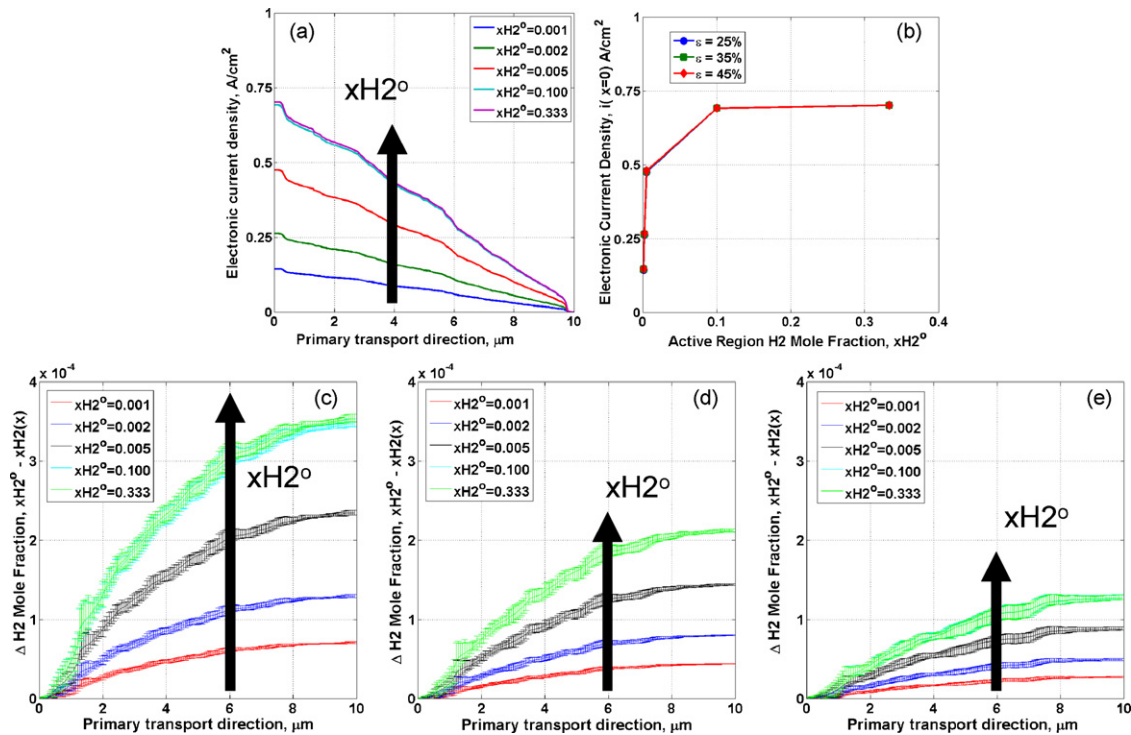
Fig. 9. The effect of concentration limitations in the interlayer at a constant $\eta = 400$ mV overpotential. Equilibrium mole fractions are kept consistent with Table 2 and the N_2 mole fraction is held constant in all studies of, 0.334. (a) The electronic current density is shown along the primary transport direction for the structure with a porosity of 25%, and maintaining interlayer inlet H_2 mole fractions, $x_{H_2}^0$, approaching zero. (b) The maximum electronic current density for the structures with a porosity of 25%, 35%, and 45%, respectively, as a function of the interlayer inlet H_2 mole fraction. Changes in mean H_2 mole fraction are shown with scatter-bars representing the maximum and minimum span-wise (y-direction) variations for the structures with a porosity of (c) 25%, (d) 35%, and (e) 45%. The direction of the increasing H_2 mole fraction in the interlayer is noted with arrows.

the remaining structures. This point is further conveyed in Fig. 9b, where the net electronic current density generated in the interlayer region is plotted as a function of the H_2 mole fraction prescribed at the interlayer inlet, where trends for the structures with a porosity of 25%, 35%, and 45%, respectively, are shown. Again, at higher inlet mole fractions, consistent results are observed; however, at lower inlet H_2 mole fractions, there is a substantial decrease in the electronic current density produced for any of the structures.

Moving to Fig. 9c through Fig. 9e, a variation parameter is plotted for the structures with a porosity of (Fig. 9c) 25%, (Fig. 9d) 35%, and (Fig. 9e) 45%, for the considered inlet H_2 mole fractions for the interlayer region. This parameter, considers the average change in H_2 mole fraction within the structures. It is calculated by subtracting the average mole fraction from the value prescribed at the interlayer inlet (i.e. $x_{H_2}^0 - \overline{x_{H_2}}(x)$), where the bar indicates that the mole fraction is averaged over the span-wise direction so that it is only a function of the primary transport direction, x. As before, the scatter-bars for each trend represent the maximum/minimum span-wise variations. In Fig. 9c through Fig. 9e, the effects of the concentration limitation are observed. At the lower inlet H_2 mole fractions, there are smaller mean variations. Further, as this inlet H_2 mole fraction is increased, the variations increase until there is sufficient H_2 that concentration limitations due to mass transfer play a minor role. Because of the reduced mass transport cross-sections in the structures with a lower porosity, these effects are amplified at lower the lower porosities.

4. Conclusions

A coupled electrochemical kinetics and LBM mass transfer model has been developed, verified, and discussed for the electrochemical oxidation of gas phase hydrogen and water in a porous Ni–YSZ cermet anode. This model is suitable for use in the examina-

tion of combined effects in electrochemically active regions of the SOFC anode. Specific attention is paid to the details of the implementation and coupling of the electrochemical kinetics with the LBM mass transfer model.

After validation of the electrochemical kinetic and mass transfer sub-models, the coupled model was used to study a single 2D pore. The interplay of electrochemistry and mass transfer is observed on a conceptual basis and demonstrated the effects of concentration limitations on the electrochemical kinetics at constant overpotential.

The model is then applied to six conceptual structures with porosities ranging from 25% to 50%. These structures were used to represent an anodic interlayer. These studies considered distributions of electrochemically active sits, which were fit in a non-dimensional manner to consistent parametric descriptions of a system. Parametric studies of the effects of the applied overpotential, porosity, and hydrogen mole fraction at the inlet of the interlayer were considered. All studies were performed assuming a constant overpotential. The constant overpotential is identified as a limiting feature of the present system, due to the large resistivity of the YSZ phase and an inability to account for the coupled transport processes. While detailed descriptions of the structure, phase paths, and their interfaces are necessary for appropriate treatment of the problem, treatment of these issues and parameterized descriptions of the dense structures will be considered (e.g. such as through percolation theory) in future studies. Additionally, the linking of localized details captured by representative volumes with the LBM will be coupled to larger cell-level models for the prescription and refinement of boundary conditions. This will ensure validity of the considered cases.

While the parametric studies presented in this work demonstrated some interesting predictive capabilities with high spatial fidelity, the overall goal of this work is to report the methods used

for coupling the mass transfer and electrochemical kinetic systems, verify its implementation, and demonstrate their use. To that end, future studies will consider more rigorous scenarios, structures, and validation with respect to experimental findings in real systems. Additionally, updates to the electrochemical mechanisms to ensure thermodynamic consistency of the kinetics will be made. Still, with the computational power to describe parallel transport and electrochemical reaction processes within details of the SOFC anode micro- to nano-structure, promises to provide an advanced understanding of processes inhibiting their performance and promoting degradation effects.

Acknowledgments

Appendix A. Lattice Boltzmann method for multicomponent diffusion

The details of the multi-component lattice Boltzmann method (LBM) being used in this work have been previously published in full detail [33,38,39]. An abbreviated discussion is provided here for clarity and completeness. Interested readers are directed to the previous publications. The multi-component LBM uses a different lattice speed (DLS) multi-species model that has been extended from the original two-species works of Luo and Girimaji as well as McCracken and Abraham [36,37]. The method is suitable for modeling mass transfer in complex structures because of the high convergence and mesh integrity that results from the kinetic basis of the method [38,41,49]. The LBM uses a regular mesh providing the ability to implement boundary conditions in an ad-hock manner as was shown in Fig. 2. This means that the method does not maintain the difficulties in meshing complex structures and geometries that plague other methods. It should be noted, that as shown here, the LBM is bound to the continuum limit. Further, it can be shown to recover the continuum transport equations [50–52]. However, because the method is a direct implementation of the Boltzmann equation, it should be tractable to extend it to the transition and non-continuum transfer regimes that find merit in the SOFC transport problem. This is an active area of research and some recent works have shown the ability to recover these processes [39]. The work presented here is found on continuum theory for a ternary transport problem.

The numerical scheme employs a discrete time marching scheme that uses the individual species densities, species velocities, mixture density, and mass averaged velocity as the independent variables. These quantities are determined by performing moment closure schemes on the particle velocity distribution function (PDF). The PDF, f_α^i, can be defined for every species 'i' moving in direction α with a velocity vector of $\vec{e_\alpha^i}$. The PDF is determined at each lattice point, $\vec{x}$, and time t. The solution is completed over a numerical grid that is comprised of discrete and regularly spaced lattice points. The PDF is solved at each lattice point on a species-by-species basis by imposing streaming and collision steps, comprising the discretized form of the Boltzmann transport equation. In combined form, these steps yield,

$$f_\alpha^i(\vec{x} + \vec{e_\alpha^i}, t + \Delta t) - f_\alpha^i(\vec{x}, t) = \Omega_\alpha^i \tag{A1}$$

where Ω_α^i is a collision integral representing self and multi-component diffusion processes and the difference between PDF terms represents the streaming process required to update the local field. For the two-dimensional, nine-directional (D2Q9) lattice model, the streaming velocity is fixed for the first species that must also be the lightest species. These velocities are defined in non-dimensional form.

$$\begin{array}{lll} e_0^1 = (0, 0) & e_1^1 = (1, 0) & e_2^1 = (1, 1) \\ e_3^1 = (0, 1) & e_4^1 = (-1, 1) & e_5^1 = (-1, 0) \\ e_6^1 = (-1, -1) & e_7^1 = (0, -1) & e_8^1 = (1, -1) \end{array} \tag{A2}$$

Employing the DLS scheme, the heavier species use these streaming velocities as a reference frame [37,38]. Using an isothermal assumption, it can be resolved that the streaming velocities can be found,

$$\vec{e_\alpha^2} = \vec{e_\alpha^1} \sqrt{\frac{MW_1}{MW_2}} \qquad \vec{e_\alpha^3} = \vec{e_\alpha^1} \sqrt{\frac{MW_1}{MW_3}} \tag{A3}$$

where MW_i represents the molecular weight of species i. Because of these different streaming velocities, the second and third species will stream off of the lattice grid set using the first, lightest species. To reconcile this difference in streaming conditions for the heavier species, bilinear interpolation is applied to interpolate the PDF quantities. This provides the values for the second and third species corresponding to the locations of the original lattice grid [37,38].

The macroscopic transport properties, namely the concentrations, densities and the velocities, are obtained by completing moment closures on the PDF quantities. The number density for species i, n_i, is obtained by,

$$n_i = \sum_{\alpha=0}^{8} f_\alpha^i \tag{A4}$$

at any given lattice point. The total system number density can then be obtained by summing across species.

$$n = n_1 + n_2 + n_3 \tag{A5}$$

To convert number density into a mass density of species i, ρ_i, and net density, ρ, the molecular weight of species i is employed,

$$\rho_i = MW_i \cdot n_i \tag{A6}$$

$$\rho = \rho_1 + \rho_2 + \rho_3 \tag{A7}$$

where the appropriate molar conversions have been completed.

Similarly, the species velocities $\vec{u_i}$ can be determined using a second moment closure,

$$n_i \cdot \vec{u_i} = \sum_{\alpha=0}^{8} f_\alpha^i \cdot \vec{e_\alpha^i} \tag{A8}$$

where this component velocity, along with a mass averaged velocity and component number densities, will be used in the equilibrium distribution function that is a discretized form of a Maxwellian distribution. A second species velocity, $\vec{u_i'}$, is used to compute the mole fluxes in addition to the flux and concentration boundary conditions that are used in this study,

$$4n_i \cdot \vec{u_i} = \left(4 - \frac{1}{\tau_{ij}} - \frac{1}{\tau_{ik}}\right) \sum_{\alpha=0}^{8} f_\alpha^i \cdot \vec{e_\alpha^i} + \left(\frac{1}{\tau_{ij}} + \frac{1}{\tau_{ik}}\right) \sum_{\alpha=0}^{8} f_\alpha^{i,eq} \cdot \vec{e_\alpha^i} \tag{A9}$$

$$\vec{J_i} = n_i \cdot \vec{u_i'} \tag{A10}$$

where τ_{ij} is the relaxation parameter, $f_\alpha^{i,eq}$ the equilibrium distribution for species i in direction α, and $\vec{J_i}$ is the species molar flux

vector. Prior to discussion of the equilibrium distribution and relaxation parameter, the standard mass average velocity is defined.

$$\rho \cdot \vec{u} = \rho_1 \cdot \vec{u_1} + \rho_2 \cdot \vec{u_2} + \rho_3 \cdot \vec{u_3} \tag{A11}$$

Using the individual species velocities, mass average velocity, and species number densities, the equilibrium distribution function that represents the Maxwellian distribution is shown as,

$$f_\alpha^{i,eq} = \omega_\alpha n_i \left[1 + \frac{\vec{e_\alpha^i} \cdot \vec{u}}{c_{s,i}^2} + \frac{(\vec{e_\alpha^i} \cdot \vec{u})^2}{2c_{s,i}^4} - \frac{\vec{u} \cdot \vec{u}}{2c_{s,i}^2} \right] \tag{A12}$$

$$f_\alpha^{i(0)} = f_\alpha^{i,eq} \left[1 + \frac{(\vec{e_\alpha^i} - \vec{u}) \cdot (\vec{u_i} - \vec{u})}{c_{s,i}^2} \right] \tag{A13}$$

where ω_α are weight functions arising from the discretization process and $c_{s,i}$ is the non-dimensional speed of sound for species i:

$$\omega_0 = \frac{4}{9}; \omega_1 = \omega_3 = \omega_5 = \omega_7 = \frac{1}{9}; \omega_2 = \omega_4 = \omega_6 = \omega_8 = \frac{1}{36} \tag{A14}$$

$$c_{s,1} = \frac{1}{\sqrt{3}}, c_{s,2} = c_{s,1} \cdot \sqrt{\frac{MW_1}{MW_2}}, c_{s,3} = c_{s,1} \cdot \sqrt{\frac{MW_1}{MW_3}} \tag{A15}$$

The weight functions are unique for individual lattice configurations. The unique speed of sound for the individual species is a result of the DLS approach and required for consistent definition within the LBM structure.

With the equilibrium distribution functions, the collision processes are determined. As shown in Eq. (A1), the collision terms are treated on a species-by-species basis in direction α. This collision process is broken down into self-collisions, representative of self diffusion and bulk-viscous fluid motion, and inter-species collisions that are representative of molecular diffusion processes. As a result, for the ternary system, the collision terms take on the form.

$$\begin{aligned} \Omega_\alpha^1 &= \Omega_\alpha^{11} + \Omega_\alpha^{12} + \Omega_\alpha^{13}, \\ \Omega_\alpha^2 &= \Omega_\alpha^{21} + \Omega_\alpha^{22} + \Omega_\alpha^{23}, \\ \Omega_\alpha^3 &= \Omega_\alpha^{31} + \Omega_\alpha^{32} + \Omega_\alpha^{33} \end{aligned} \tag{A16}$$

The self-collision terms can be evaluated as,

$$\Omega_\alpha^{ii} = -\left(\frac{f_\alpha^i - f_\alpha^{i(0)}}{\tau_i} \right) \tag{A17}$$

and τ_i is the viscous relaxation term. The cross-collision terms represent collision processes between different species. It is the dominant collision process in diffusion dominated flow and is expressed as.

$$\Omega_\alpha^{ij} = -\frac{1}{\tau_{ij}} \left(\frac{\rho_j}{\rho} \right) \frac{f_\alpha^{i,eq}}{c_{s,1}^2} (\vec{e_\alpha^i} - \vec{u}) \cdot (\vec{u_i} - \vec{u_j}) \tag{A18}$$

Following a complex hydrodynamic closure scheme, the cross-collision relaxation terms can be correlated to diffusion coefficients by the expression,

$$D_{ij} = \frac{\rho \cdot P}{n^2 \cdot MW_i \cdot MW_j} \cdot \left(\tau_{ij} - \frac{1}{2} \right) \tag{A19}$$

where the total pressure in this expression, P, is consistent with that from kinetic theory,

$$P = \rho_1 \cdot c_{s,1}^2 + \rho_2 \cdot c_{s,2}^2 + \rho_3 \cdot c_{s,3}^2 \tag{A20}$$

and using Eqs. (A20) and (A15) it is shown that,

$$P = \frac{MW_1 \cdot n}{3} \tag{A21}$$

Following the manipulation of Eqs. (A19–A21), the cross-collision relaxation term at discrete lattice points can be found on the basis of specified diffusivities.

$$\tau_{ij} = \frac{1}{2} + 3D_{ij} \frac{MW_i \cdot MW_j}{M_1} \left(\frac{n}{\rho} \right) \tag{A22}$$

At this point it should be noted that to maintain numeric stability with the LBM, both τ_{ij} and τ_i require to be on the order of unity. Given the system constraints, non-dimensional scaling is used to maintain this requirement and model physically relevant processes. This has been standard practice within the LBM methodology. The details of the scaling are provided within the body of the text during discussion of implementation of the models.

Appendix B. Implementation of the LBM boundary conditions

Implementation of discrete Neumann and Dirichlet boundary conditions at specific boundary nodes is necessary for the implementation of the electrochemical kinetics model within the LBM mass transfer framework. Fig. B1 provides a conceptual schematic of the types of structures that boundary conditions are necessary for. In Fig. B1, the dark region can either represent the edge of a Dirichelt boundary (e.g. an inlet) and/or a region of the dense materials. Depending upon its numeric identification, as discussed with Fig. 2, all of the dense regions will either be considered as impermeable or as electrochemically active with an empirical correction for a mean field description of the system's electrochemical interface (i.e. TPB length and active width from the TPB). Treatment of these boundary conditions is necessary.

We begin this discussion with the description of a Dirichelt condition, for geometry comparable to that shown in Fig. B1a. This discussion is limited to the 2D, 9-direciton LBM representation, but is readily extended to multiple dimensions. In the studies performed, concentrations are specified for the pore regions along the domain inlet. The Dirichlet boundary condition associated with this property has previously been reported by the authors [38]. For consistency a brief description is provided here. In short, the particle velocity equation, Eq. (A9), is used in a manner resembling that first introduced by Zou and He [53]. To this effect, we introduce a base velocity correction for each species, $\overline{u_i'} = \vec{u_i} \sqrt{M_i/M_1}$, and

$$4n \cdot \overline{u_x'} = (4-\phi) \cdot \left[(f_1^i + f_2^i + f_8^i) - (f_4^i + f_5^i + f_6^i) \right] \\ + \phi \cdot \left[(f_1^{i(eq)} + f_2^{i(eq)} + f_8^{i(eq)}) - (f_4^{i(eq)} + f_5^{i(eq)} + f_6^{i(eq)}) \right] \tag{B1}$$

$$4n \cdot \overline{u_y'} = (4-\phi) \cdot \left[(f_2^i + f_3^i + f_4^i) - (f_6^i + f_7^i + f_8^i) \right] \\ + \phi \cdot \left[\left(f_2^{i(eq)} + f_3^{i(eq)} + f_4^{i(eq)} \right) - (f_6^{i(eq)} + f_7^{i(eq)} + f_8^{i(eq)}) \right] \tag{B2}$$

where (eq) denotes the equilibrium PDF values in the noted PDF direction, as defined by Eq. (A12). A relaxation parameter, φ, which for a 3-species mixture is defined as,

$$\phi = \left(\frac{1}{\tau_{ij}} + \frac{1}{\tau_{ik}} \right) \tag{B3}$$

where τ_{ij} represents the diffusive relaxation times. Using Eqs. (B1–B3) with the number density moment equation, Eq. (A4), the unknown PDF values can be determined. In practice, the x-component of the particle density is specified for defining a concentration boundary node at $x = 0$. This leaves unknown PDF values
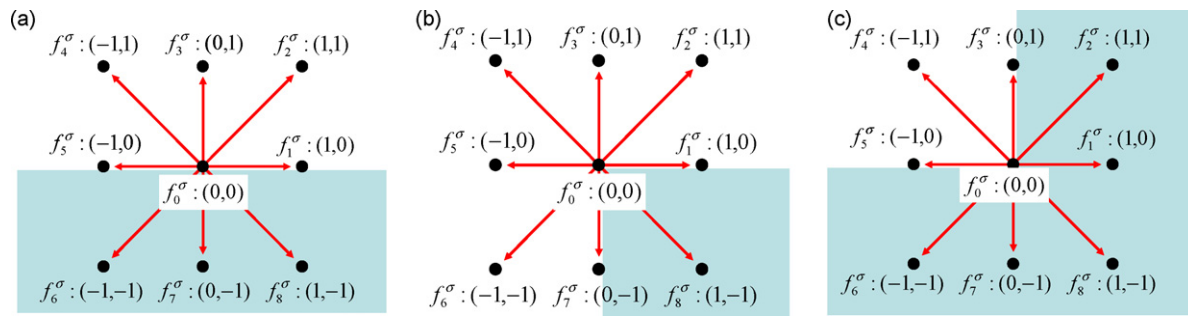
Fig. B1. Boundary condition schematics: (a) flat boundary; (b) convex boundary; (c) concave boundary.

of f_1^i, f_2^i, and f_8^i at $x = 0$ with a normal facing in the positive direction into the domain. Through some manipulation,

$$(f_1^i + f_2^i + f_8^i) = n^i - (f_0^i + f_3^i + f_4^i + f_5^i + f_6^i + f_7^i) \tag{B4}$$

$$(f_1^i + f_2^i + f_8^i) = (f_4^i + f_5^i + f_6^i)$$
$$+ \left[\frac{4n \cdot \overrightarrow{u_x} - \phi \left[(f_1^{i(eq)} + f_2^{i(eq)} + f_8^{i(eq)}) - (f_4^{i(eq)} + f_5^{i(eq)} + f_6^{i(eq)}) \right]}{(4 - \phi)} \right] \tag{B5}$$

$$(f_2^i - f_8^i) = f_6^i + f_7^i - f_3^i - f_4^i$$
$$+ \left[\frac{4n \cdot \overrightarrow{u_y} - \phi \left[(f_2^{i(eq)} + f_3^{i(eq)} + f_4^{i(eq)}) - (f_6^{i(eq)} + f_7^{i(eq)} + f_8^{i(eq)}) \right]}{(4 - \phi)} \right] \tag{B6}$$

where Eqs. (B4–B6) are used to show that the number density can be determined as a function of the particle velocity. Defining f_1^i with the Zou and He approach [53],

$$f_1^i = f_5^i + \left(f_1^{i(eq)} - f_5^{i(eq)} \right) = f_5^i + \frac{2n \cdot \overrightarrow{u_x}}{9C_{s,i}^2} \tag{B7}$$

where the mass average velocity is used in Eq. (B7). Substituting Eq. (B7) into Eq. (B6),

$$(f_2^i + f_8^i) = f_4^i f_6^i - \frac{2n \cdot \bar{u}_x}{9C_{s,i}^2}$$
$$+ \left[\frac{4n \cdot \bar{u}_x' - \phi \left[(f_2^{i(eq)} + f_3^{i(eq)} + f_4^{i(eq)}) - (f_6^{i(eq)} + f_7^{i(eq)} + f_8^{i(eq)}) \right]}{(4 - \phi)} \right] \tag{B8}$$

where all PDF values, and thus the number density or concentration, and momentum moments are closed for the system.

The Neumann or flux boundaries can be defined by using the same system of equations as the Dirichlet boundaries. The primary difference is that the particle velocities are explicitly defined for the system of equations rather than the concentration.

In the 2D, 9-direction lattice used in this study, this system of equations can be derived for the 4-normal directions corresponding to the Cartesian x- and y-directions. Because the electrochemical oxidation kinetics mechanism is used to define a unique flux at each discrete node which is defined as active, the velocity is a function of the location within the geometry in this study. However, as shown in Fig. B1b and c, the rectangular LBM grid also requires treatment of four concave and four convex boundaries. A similar development to those shown for the Cartesian directions can be shown for the convex boundaries, with the appropriate weighting functions. The

PDF in the directions tangent to each respective corner is allowed to propagate and relax without manipulation from the boundary condition, but the general procedure is consistent. Concave boundaries, like that in Fig. B1c, are indeterminate in the present scheme and limited to a bounce-back, or zero flux condition. It is possible to do flux extrapolation and correction to neighboring nodes based upon an area weighting; however, this is not considered in the present study. Bounce-back boundary conditions have been previously discussed [38].

References

[1] S.C. Singhal, K. Kendall, High-Temperature Solid Oxide Fuel Cells: Fundamentals, Design and Applications, Elsevier Advanced Technology, Oxford, 2003.
[2] W.Z. Zhu, S.C. Deevi, Mater. Sci. Eng. A 362 (2003) 228–239.
[3] H. Xiao, T.L. Reitz, M.A. Rottmayer, J. Power Sources 183 (2008) 49–54.
[4] H. Yokokawa, H. Tu, B. Iwanschitz, A. Mai, J. Power Sources 182 (2008) 400–412.
[5] C. Sun, U. Stimming, J. Power Sources 171 (2007) 247–260.
[6] A.V. Virkar, J. Chen, C.W. Tanner, J.-W. Kim, Solid State Ionics 131 (2000) 189–198.
[7] G.J. Offer, D.J.L. Brett, N.P. Brandon, ECS Trans. 7 (2007) 1645–1652.
[8] Y. Jiang, A.V. Virkar, F. Zhao, J. Electrochem. Soc. 148 (2001) A1091–A2099.
[9] J. Divisek, R. Jung, I.C. Vinke, J. Appl. Electrochem. 29 (1999) 165–170.
[10] S.H. Chan, Z.T. Xia, J. Electrochem. Soc. 148 (2001) A388–A394.
[11] S. Primdahl, M. Mogensen, J. Electrochem. Soc. 144 (1997) 3409–3419.
[12] M. Brown, S. Primdahl, M. Mogensen, J. Electrochem. Soc. 147 (2000) 475–485.
[13] H. Zhu, R.J. Kee, J. Electrochem. Soc. 155 (2008) B715–B729.
[14] F. Zhao, A.V. Virkar, J. Power Sources 141 (2005) 79–95.
[15] A. Bieberle, L.J. Gauckler, Solid State Ionics 146 (2002) 23–41.
[16] W.G. Bessler, Solid State Ionics 176 (2005) 997–1011.
[17] M. Mogensen, J. Høgh, K.V. Hansen, T. Jacobsen, ECS Trans. 7 (2007) 1329–1338.
[18] W.G. Bessler, J. Warnatz, D.G. Goodwin, Solid State Ionics 177 (2007) 3371–3383.
[19] D.G. Goodwin, Proc. Electrochem. Soc. PV 2005–07 (2005) 699–707.
[20] A.S. Joshi, K.N. Grew, J.R. Izzo Jr., A.A. Peracchio, W.K.S. Chiu, ASME J. Fuel Cell Sci. Technol. 7 (2010) 011006.
[21] J.R. Izzo Jr., A.S. Joshi, K.N. Grew, W.K.S. Chiu, A. Tkachuk, S.H. Wang, W. Yun, J. Electrochem. Soc. 155 (2008) B504–B508.
[22] K.N. Grew, J.R. Izzo Jr., W.K.S. Chiu, ECS Trans. 13 (2008) 123.
[23] J.R. Wilson, S.A. Barnett, Electrochem. Solid State Lett. 11 (2008) B181–B185.
[24] J.R. Wilson, W. Kobsiriphat, R. Mendoza, H.-C. Chen, T. Hines, J.M. Hiller, D.J. Miller, K. Thornton, P.W. Voorhees, S.B. Adler, D. Mumm, S.A. Barnett, ECS Trans. 7 (2007) 1879–1887.
[25] J.R. Wilson, W. Kobsiriphat, R. Mendoza, H.-C. Chen, J.M. Hiller, D.J. Miller, K. Thornton, P.W. Voorhees, S.B. Adler, S.A. Barnett, Nat. Mater. 5 (2006) 541–544.
[26] M. Vogler, A. Bieberle-Hütter, L. Gauckler, J. Warnatz, W.G. Bessler, J. Electrochem. Soc. 156 (2009) B663–B672.
[27] H. Zhu, R.J. Kee, V.M. Janardhanan, O. Deutschmann, D.G. Goodwin, J. Electrochem. Soc. 152 (2005) A2427–A2440.
[28] D.G. Goodwin, H. Zhu, A.M. Colclasure, R.J. Kee, J. Electrochem. Soc. 156 (2009) B1004–B1021.
[29] K. Christmann, Surf. Sci. Rep. 9 (1988) 1–163.
[30] W.G. Bessler, S. Gewies, M. Vogler, Electrochim. Acta 53 (2007) 1782–1800.
[31] S. Gewies, W.G. Bessler, J. Electrochem. Soc. 155 (2008) B937–B952.
[32] H.S. Fogler, Elements of Chemical Reaction Engineering, fourth ed., Prentice Hall PTR, Upper Saddle River, NJ, 2006.
[33] A.S. Joshi, K.N. Grew, A.A. Peracchio, W.K.S. Chiu, J. Power Sources 164 (2007) 631–638.
[34] R.J. Kee, M.E. Coltrin, P. Glarborg, Chemically Reacting Flow, Wiley-Interscience, Hoboken, NJ, 2003.
[35] W.G. Bessler, S. Gewies, J. Warnatz, Proc. Electrochem. Soc. PV 2005–07 (2005) 708–718.
[36] L.-S. Luo, S.S. Girimaji, Phys. Rev. E 67 (2003) 036302.
[37] M.E. McCracken, J. Abraham, Phys. Rev. E 71 (2005) 036701.

[38] A.S. Joshi, A.A. Peracchio, K.N. Grew, W.K.S. Chiu, J. Phys. D 40 (2007) 2961–2971.
[39] A.S. Joshi, A.A. Peracchio, K.N. Grew, W.K.S. Chiu, J. Phys. D 40 (2007) 7593–7600.
[40] X. Shan, G. Doolen, Phys. Rev. E, 54 (1996) 3614–3620.
[41] M.C. Sukop, D.T. Thorne, Lattice Boltzmann Modeling, Springer, New York, 2006.
[42] D. Chen, Z. Lin, H. Zhu, R.J. Kee, J. Power Sources 191 (2009) 240–252.
[43] P. Costamagna, M. Panizza, G. Cerisola, A. Barbucci, Electrochim. Acta 47 (2002) 1079–1089.
[44] S. Sunde, J. Electrochem. Soc. 143 (1996) 1930–1939.
[45] P. Costamagna, P. Costa, V. Antonucci, Electrochim. Acta 43 (1998) 375–394.
[46] S.C. DeCaluwe, H. Zhu, R.J. Kee, G.S. Jackson, J. Electrochem. Soc. 155 (2008) B538–B546.
[47] P. Asinari, M.C. Quaglia, M.R. Von Spakovsky, B.V. Kasula, J. Power Sources 170 (2007) 359–375.
[48] R.B. Bird, W.E. Stewart, E.N. Lightfoot, Transport Phenomena, second ed., J. Wiley, New York, 2002.
[49] S. Chen, G.D. Doolen, Ann. Rev. Fluid Mech. 30 (1998) 329–364.
[50] X. He, L.-S. Luo, Phys. Rev. E 56 (1997) 6811–6817.
[51] X. He, L.-S. Luo, Phys. Rev. E 55 (1997) R6333–R6336.
[52] X. He, L.-S. Luo, J. Stat. Phys. 88 (1997) 927–944.
[53] Q. Zou, X. He, Phys. Fluids 9 (1997) 1591–1596.